Nanoscale Advances

ROYAL SOCIETY OF CHEMISTRY

PAPER

View Article Online
View Journal

Cite this: DOI: 10.1039/d5na00943j

Plasmon-boosted S-scheme g-C_3N_4–Co_3O_4–Ag 2D nanostructure for highly efficient visible-light antibacterial photocatalysis

Sanaa Mohammed Abdu Kaid,†[a] Khaled Alkanad,†[bi] Nael Abutaha,[c] Fahd A. Al-Mekhlafi,[c] Abishad Padikkamannil,[d] Mohammed A. Bajiri,[e] Maged Alkanad,[f] Mohamed Masri,[h] Yusuf Olatunji Waidi,[g] Prashantha Kalappa,[a] Upendra N.*[a] and Lokanath N. K.*[b]

The rapid emergence of multidrug-resistant bacteria has created an urgent need for safe and efficient antimicrobial strategies. Here, we present a rationally engineered 2D plasmonic photocatalyst based on g-C_3N_4 nanosheets coupled with Co_3O_4 and Ag nanoparticles to construct an S-scheme heterojunction. The ternary g-C_3N_4–Co_3O_4–Ag (GCA) nanocomposite was successfully fabricated, as confirmed by XRD, TEM, and SEM analyses, while UV-Vis DRS revealed the strong surface plasmon resonance (SPR) effect of Ag. The charge-transfer pathway was validated by XPS, ESR, and radical-trapping experiments, demonstrating the efficiency of the S-scheme mechanism in promoting charge separation and reactive oxygen species (ROS) generation. Under visible LED irradiation, the GCA nanocomposite exhibited outstanding antibacterial activity against methicillin-resistant *Staphylococcus aureus* (MRSA), non-typhoidal *Salmonella enteritidis* (NTS), and enteroaggregative *Escherichia coli* (EAEC), with MIC and MBC values of 140 and 280 μg mL^{-1}, respectively. The photocatalytic disinfection efficiency significantly surpassed that of pristine g-C_3N_4 and binary g-C_3N_4–Co_3O_4 composites. Importantly, negligible antibacterial effects were observed under dark conditions, underscoring the material's safety and selectivity. This study highlights the synergistic contribution of plasmonic Ag and S-scheme heterojunction engineering in enhancing visible-light-driven antibacterial performance. The findings provide a promising pathway for the development of advanced photocatalytic nanomaterials aimed at controlling healthcare-associated infections and addressing the global challenge of antibiotic resistance.

Received 4th October 2025
Accepted 10th February 2026

DOI: 10.1039/d5na00943j

rsc.li/nanoscale-advances

1. Introduction

The escalating global threat of bacterial infections, exacerbated by the rise of antibiotic-resistant strains, affects hospitals worldwide and poses significant health challenges in societies. These infections have raised concerns among healthcare providers due to their serious impact on health and economics.[1,2] Based on a recent World Health Organisation projection, if proper mitigation is not done, antibiotic-resistant bacteria might result in 10 million fatalities yearly and economic losses of US$100 trillion by 2050.[1,3] Therefore, novel approaches to biological activity treating infectious microorganisms are being developed rapidly, despite triggering antibiotic resistance.[4–6] Bacteria extermination triggered by light showcases distinct benefits, functioning through either oxidative harm triggered by the generation of reactive oxygen species (ROSs) or thermal stress from elevated temperatures, processes known as photodynamic and photothermal therapies, respectively.[7,8] Photocatalysis is a promising method due to its strong redox reactions, providing large amounts of ROSs, which leads to high antibacterial activity with straightforward/non-toxic byproducts.[9–11] Moreover, photocatalytic antibacterial methodologies leverage clean and readily available solar energy, offering a swift, effective, and less likely antibiotic resistance-inducing solution.[5,12] However, photocatalyst efficiency

[a]Center for Research and Innovations, Faculty of Natural Sciences, Adichunchanagiri University, B. G. Nagar, Karnataka, 571448, India. E-mail: nupendra90@gmail.com
[b]Department of Studies in Physics University of Mysore Manasagangotri, Mysuru 570 006, India. E-mail: lokanath@physics.uni-mysore.ac.in
[c]Department of Zoology, College of Science, King Saud University, Riyadh 11451, Saudi Arabia
[d]Department of Studies and Research in Microbiology, Mangalore University, Karnataka, India
[e]Instituto de Física de São Carlos, Universidade de São Paulo, São Carlos-SP, 13566-590, Brazil
[f]Department of Pharmacognosy, Sri. Adichunchanagiri College of Pharmacy, Adichunchanagiri University, B. G. Nagara, Mandya, Karnataka, 571448, India
[g]Department of Materials Engineering, Indian Institute of Science, Bangalore 560012, India
[h]Center for Research and Innovations, BGS Institute of Technology, Adichunchanagiri University, B. G. Nagar, Karnataka, India
[i]Industrial Chemistry and Heterogeneous Catalysis, Department of Chemistry, TUM School of Natural Sciences, Technical University of Munich, Garching, 85748, Germany
† These authors contributed equally to this work.

depends on numerous factors, including band edge location, narrow bandgap energy, decreased charge recombination, improved charge separation and transfer, and surface-active sites.[13]

Lately, two-dimensional (2D) photocatalysts have gained growing interest owing to their remarkable optical and optoelectronic advantages, leading to diverse applications.[14,15] The increased attention is a result of the abundance of active sites afforded by low-coordinated atoms at the borders and edges of grains of 2D semiconductors, which interact intensely with light.[16] Despite their promised photocatalytic properties, pure 2D semiconductors encounter challenges such as layered reassembling. This limits their ability to absorb light and charge dynamics, leading to a high electron–hole (e^-/h^+) recombination rate. Consequently, they have a low photonic cross-section and a poor quantum yield. Nonetheless, the electronic structures of the 2D semiconductor may be modified by doping, coupling, or surface integration of the intrinsically passivated interfaces with diverse low-dimensional photonic nanostructures. Developing 2D-based hybrid nanocomposites improves photocatalytic capabilities by offering greater charge generation, better interfacial charge separation, numerous active sites, and strong redox abilities.[9,17] Recently, the S-scheme heterojunction has been invented due to its advantages over other heterojunction configurations.[18] These hybrid S-scheme nanocomposites provide better charge separation under light illumination for enhanced antibacterial activity.[19]

Additionally, incorporating plasmonic metals boosts photocatalytic efficiency by enhancing light–matter interaction through the migration of surface plasmon polaritons (SPPs) or localised surface plasmon resonance (LSPR).[19] This enhancement is not achievable with non-plasmonic metals because of their limited ability to absorb light, mostly resulting from interband shifts. In addition, using hot carriers generated by plasmon non-radiative decay enhances both the photochemical reaction efficiency and selectivity, even when subjected to low-intensity illumination. Plasmonic metals can also serve as co-catalysts, providing more active sites through electron capture, extending the lifespan of plasmonic e^-/h^+ pairs, and facilitating photocatalytic processes under thermal and nonthermal methods.[20]

Among various 2D semiconductors, graphitic carbon nitride nanosheets (g-C_3N_4 NSHs) have exclusive properties, such as n-type conductivity with ultraviolet-visible absorption ability and a bandgap value of 2.7 eV, appropriate charge transport capabilities, and numerous active sites.[21,22] 2D g-C_3N_4 has been extensively studied and has shown great promise as a photocatalytic antibacterial nanomaterial against clinically isolated, multi-drug resistant microorganisms due to the material's proficiency, stability, and environmental sustainability.[23] However, pristine g-C_3N_4 has limited photocatalytic activity attributed to the low valence band (VB) potential and fast recombination rate of photoinduced charge carriers. Thus, to construct an effective heterojunction photocatalyst, it is crucial to select semiconductors with matched bandgap configurations and maintain an intimately interconnected interface between the two components.[13] In this context, cobalt oxide nanoparticles (Co_3O_4 NPs) are a highly desirable p-type semiconductor with a direct optical bandgap of 2.44 eV. These NPs have great promise for many applications, such as photocatalytic processes, pharmacology, biomedical visualisation, cancer treatment, and chemical sensing.[24–29] Considering the band structures, Co_3O_4 and g-C_3N_4 are found to be promising photocatalysts to form an S-scheme heterojunction, which enables them to facilitate both oxidation and reduction reactions concurrently.[21,30,31] Recent studies have shown that the coupling of Co_3O_4 and g-C_3N_4 nanostructures forms nanoheterostructures with higher photocatalytic activity.[32,33]

Beyond semiconductor coupling, the deposition of noble metals (such as platinum, gold, or silver) on the heterostructure surface can develop multiple photocatalytic mechanisms for enhanced antibacterial activity.[34] Ag NPs are great candidates for effective photocatalytic antibacterial systems given their strong local electromagnetic fields, excellent optical absorption, and cost-effective advantages.[35] The suitable Fermi level of the Ag NPs with the Fermi levels of g-C_3N_4 NSHs and Co_3O_4 NPs induces a shift in their band levels once combined, forming double Schottky barriers. The SPR effect of the Ag NPs results in e^-/h^+ pair transformation over the Schottky junctions to more negative potentials, facilitating e^-/h^+ pair separation and increasing the quantum efficiency of the g-C_3N_4–Co_3O_4 heterostructure. Hence, this process maintains the redox ability of electrons that migrated to the conduction band (CB) of g-C_3N_4 and holes on the VB of Co_3O_4.

Recent advances in visible-light photocatalytic antibacterial systems have demonstrated the effectiveness of hybrid architectures. For example, g-C_3N_4/ZnO_2 hybrids exhibited enhanced ROS generation and improved Gram-positive bacterial inactivation under visible light.[36] Graphene oxide-supported CeO_2 composites showed reduced bandgap energy and superior antimicrobial activity under solar irradiation.[37] Green-synthesised Ag nanoparticles have also demonstrated dual antibiofilm and photocatalytic disinfection capabilities against multidrug-resistant pathogens.[38] In addition, engineered nanostructures designed to stabilise Ag nanoparticles have recently gained attention; notably, the c-Fe_2O_3@C/PIDA nanosphere system effectively stabilised Ag nanoparticles and exhibited enhanced bioactivity and antimicrobial performance through controlled Ag exposure and improved interfacial interactions.[39] Additionally, TiO_2-based/Ag visible-light photocatalysts have achieved complete inactivation of *E. coli via* ROS pathways under visible irradiation;[40,41] however, the requirement for peroxymonosulfate co-oxidants and the absence of an S-scheme heterojunction limit their broader applicability. While graphene-oxide-mediated Ag_2O nanocomposites have shown plasmon-assisted antibacterial activity,[42] the rational integration of a 2D S-scheme heterojunction with plasmonic enhancement for antibacterial photocatalysis remains underexplored, particularly against clinically isolated multidrug-resistant bacteria.[43]

In this work, we report a novel 2D plasmonic S-scheme g-C_3N_4/Co_3O_4/Ag nanocomposite designed for efficient visible-light-driven photocatalytic disinfection. Unlike previously reported systems based on type-II heterojunctions or single-

component plasmonic modification, the present strategy synergistically integrates p–n S-scheme charge transfer with Ag-induced plasmonic enhancement, enabling strong redox preservation, efficient charge separation, and sustained ROS generation. As a result, the proposed nanocomposite exhibits superior antibacterial performance, recyclability, and photocatalytic stability against clinically isolated multidrug-resistant pathogens, including methicillin-resistant *Staphylococcus aureus*, non-typhoidal *Salmonella Enteritidis*, and enteroaggregative *Escherichia coli*. This study provides a rational design framework for advanced photocatalytic disinfectants and addresses key challenges associated with antibiotic resistance and long-term antimicrobial efficacy.

2. Experimental

2.1. Chemical reagents

The laboratory-grade chemicals were $Co(NO_3)_2 \cdot 6H_2O$, $AgNO_3$ (Alfa Aesar), urea, glycine (Sigma Aldrich), Baird-Parker (BP) agar, Xylose Lysine Deoxycholate (XLD) agar, Eosin Methylene Blue (EMB) agar, Mueller–Hinton broth (cation-adjusted) (MHB-CA), and resazurin sodium (Himedia, India). In the examinations, 18.2 MΩ cm of ultrapure water was also used.

2.2. Preparation of g-C_3N_4 NSHs

In a crucible, 10 g of urea was calcined for three hours. The first hour was at 200 °C, the second hour was at 400 °C, and the third hour was at 550 °C. A yellowish g-C_3N_4 powder was obtained and labelled "G" for further studies.

2.3. Preparation of Co_3O_4 NPs

Co_3O_4 was prepared by solution combustion. A 0.1 M amount of $Co(NO_3)_2 \cdot 6H_2O$ was dissolved in 50 mL of ultrapure water and mixed for 30 min in a hotplate stirrer. Then, 0.1 M glycine as fuel was added (fuel and oxidiser ratio maintained to be one), and the temperature was raised to 350 °C until it ignited and burned with a bright flame. A fine powder was produced and calcined in a furnace oven for 1 hour at 500 °C. Co_3O_4 nanoparticles were obtained and labelled as "C" for the other analyses.

2.4. Preparation of the g-C_3N_4–Co_3O_4 nanocomposite

The binary g-C_3N_4–Co_3O_4 nanocomposite was prepared by grinding 40 mg of Co_3O_4 with 10 g of urea for 30 minutes. A fine powder mixture was obtained and treated similarly to the preparation of pristine g-C_3N_4. The formed g-C_3N_4–Co_3O_4 nanocomposite was kept in a clean vial labelled "GC".

2.5. Preparation of the g-C_3N_4–Co_3O_4–Ag nanocomposite

The photo-deposition method was used to fabricate the g-C_3N_4–Co_3O_4–Ag nanocomposite. Exactly 0.5 g of the binary g-C_3N_4–Co_3O_4 nanocomposite was stirred in a mixture of ultrapure water and ethanol (50 mL, 1 : 1). Later, the prepared suspension was added with 1 mL (0.1 M) of $AgNO_3$ and exposed to a metal halide lamp for an hour to allow Ag^+ ions to adhere to the surface. The attained sample was rinsed many times with ultrapure water and kept to air dry at ambient temperature. The dried powder was again exposed to a metal halide lamp for 30 minutes to ensure the conversion of Ag^+ into Ag^0 nanoparticles. Finally, the sample was thoroughly rinsed with ethanol and ultrapure water to eliminate any remaining free Ag^+ ions; then, it was desiccated in a vacuum oven overnight at 60 °C, collected, and stored in a clean vial labelled "GCA" for further studies.

2.6. Characterisation

The structure of the samples was evaluated with X-ray diffraction (XRD) using a Cu Kα radiation source (Rigaku, Japan). The chemical compositions were examined with an X-ray photoelectron spectrometer (XPS, Thermo ESCALAB 250Xi, USA). The morphology and intimate contact between the NPs and NSHs were studied using scanning electron microscopy (SEM, S3400N) and transmission electron microscopy (TEM, Jeol/JEM 2100). The functional groups on the surface of the nanoparticles were determined using Fourier transform infrared (FTIR) spectroscopy. The UV-Vis spectra and the optical properties of the samples were verified using a Thermo Scientific Evolution 201 Spectrophotometer. The exchange rate of the charges was determined using a photoluminescence (PL, PerkinElmer LS55) spectrometer.

2.7. Antimicrobial activity

Briefly, the minimum inhibition concentration (MIC) was estimated by incubating 100 μL (1×10^7 CFU mL^{-1}) MDR isolates of methicillin-resistant *Staphylococcus aureus* (MRSA), non-typhoidal Salmonella Enteritidis (NTS) and enteroaggregative *E. coli* (EAEC) in 96-well flat-bottom microtiter plates with decreasing concentrations of the intended prepared photocatalyst load in 100 μL of MHB-CA medium for 24 hours. Subsequently, 20 μL of resazurin dye, at a concentration of 0.015%, was injected into each well to measure the amount of dye reduction (pink), which signifies the inhibition of bacterial growth. The minimum bactericidal concentration (MBC) of the studied photocatalyst was determined by seeding 10 μL of culture from each well displaying no evident growth in the suitable selective agar plates, such as BP agar (MRSA), XLD agar (NTS), and EMB agar (EAEC). In contrast, the MIC in the presence of photocatalysts had the lowest concentration with no apparent bacterial growth. The MBC concentration of photocatalysts was determined to be the minimum amount of studied photocatalysts that exhibited 99.90% death of the test culture.[44]

2.8. Photocatalytic disinfection

The photocatalytic disinfection properties of all prepared samples were evaluated against MRSA, NTS, and EAEC, where CA-MH broth was used for bacterial growth media. The broth was poured into a 24-well flat-bottom plate (Tarsons, India) with MIC concentrations of the studied photocatalyst added to the MRSA suspensions (1×10^7 CFU mL^{-1}). Visible-light irradiation was provided by an LED light source (50 W, $\lambda = 460$ nm) positioned at a fixed distance from the reaction plate, delivering a light intensity of approximately 63 400 lux at the sample

surface. All photocatalytic disinfection experiments were conducted under identical illumination conditions with a total exposure time of 2 h. The reaction temperature was maintained at 37 °C throughout the experiment to exclude thermal inactivation effects. Control experiments were performed in parallel, including bacterial suspensions without photocatalysts under LED irradiation and bacterial suspensions with photocatalysts kept in the dark, to distinguish photocatalytic disinfection from photolysis and dark toxicity effects. In addition, to check the viability of the test strains, 1 μL aliquots drawn at predetermined intervals were diluted in a series and cultured on BP agar media. These cultures were then placed in an incubator at 37 °C for 24 h, and the bacterial loads were demonstrated as $\log_{10}$ CFU mL^{-1}. All quantitative measurements were performed in triplicate, and the data are presented as mean values with standard deviation.

3. Results and discussion

3.1. Structural study

XRD investigation was applied to confirm the crystal structure of the fabricated samples (Fig. 1). The sample G displays two XRD peaks at 13.1° and 27.3°, which belong to the crystal planes (100) and (002) of pure g-C_3N_4 (JCPDS 87-1526), respectively. These peaks are likely attributed to the construction of the tri-*s*-triazine unit, which has a conjugated aromatic system with interplanar spacing.[12] The diffraction patterns of sample C show that it has a spinel face-centred cubic structure belonging to Co_3O_4 (JCPDS Card No. 43-1003). The XRD pattern of the GC composite shows the presence of the highest intensity peaks of g-C_3N_4 (002) and Co_3O_4 (311), indicating the well-fabrication of the g-C_3N_4–Co_3O_4 nanocomposite. The (002) crystal plane in the GC sample showed a slight shift (Fig. 1), confirming an excellent interface heterojunction in the g-C_3N_4–Co_3O_4 nanocomposite.

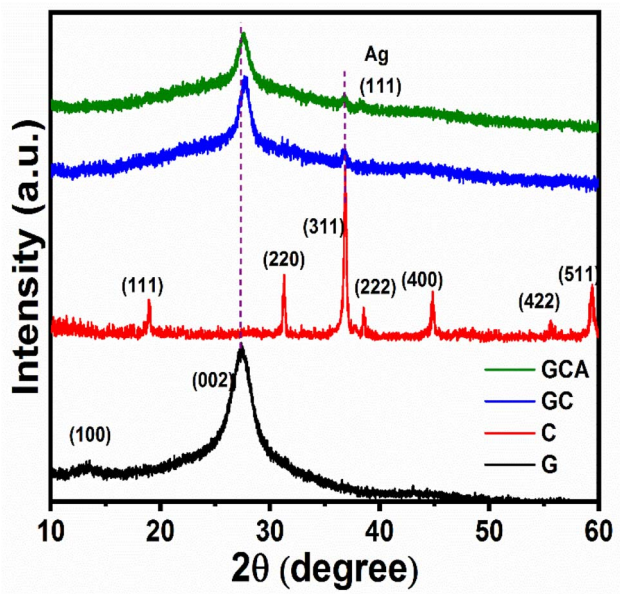

Fig. 1 XRD patterns of studied nanostructures.

This interaction between g-C_3N_4 and Co_3O_4 could slightly reduce the interfacial gap of g-C_3N_4.[13] When Ag is added to the g-C_3N_4–Co_3O_4 nanocomposite, a noticeable XRD peak at 38.16°, corresponding to the crystal plane (111) of Ag NPs (JCPDS, 04-0783), was observed in the XRD spectrum of the GCA nanocomposite, confirming the successful deposition of Ag NPs on the g-C_3N_4–Co_3O_4 nanocomposite's surface. The observed low intensity of the Ag (111) peak is attributed to both the low doping concentration of silver and its high dispersion (small particle size) within the GCA nanocomposite. Semi-quantitative EDX analysis confirms a low Ag content (1.9 atomic fraction%), which inherently results in a reduced diffraction contribution from the Ag phase (Fig. S1). Moreover, the high dispersion and nanoscale size of Ag nanoparticles lead to peak broadening and diminished XRD intensity, as commonly observed for well-dispersed plasmonic metals.

Importantly, the weak Ag reflection, together with the uniform Ag distribution observed in EDX mapping (Fig. 3d), indicates that Ag is finely dispersed and strongly anchored on the g-C_3N_4/Co_3O_4 heterostructure rather than forming large crystalline aggregates. This feature is beneficial for photocatalytic antibacterial activity, as it enhances interfacial charge transfer and plasmonic effects while avoiding agglomeration. However, the (002) peak in the GCA sample also showed a further slight shift, suggesting Ag's interaction on the surface of the g-C_3N_4–Co_3O_4 composite and further reduction in the interlayer gap of g-C_3N_4. The low content and uniform dispersion of Co_3O_4 and Ag NPs in the GCA composite make it difficult to detect the remaining diffraction peaks of these two materials.[14,15]

3.2. Morphological studies

The morphology of the produced materials was verified using the SEM technique. Fig. 2a displays pristine g-C_3N_4, which has an irregular geometry of layering smooth sheets. Pure Co_3O_4 shows a 3D network-like arrangement of NPs with lots of irregular pores (Fig. 2b). The morphology of the binary GC composite exhibits a frothy cotton-like structure with minimal agglomeration (Fig. 2c), whereas the ternary GCA composite showed more stacked sheets and an agglomeration structure due to deposited Ag NPs on the GC nanocomposite's surface (Fig. 2d).

The GCA nanocomposite's structure and layered shape were further confirmed using TEM analysis. Fig. 3a and b display the TEM images of the GCA sample, which show aggregation of the g-C_3N_4 NSHs with Co_3O_4 NPs and the success of the Ag NP deposition on the composite's surface. The selected area electron diffraction (SAED) patterns presented in Fig. 3b show lots of intense and bright circular spots, indicating the existence of heavy atoms in the heterostructure.[45] Hence, SAED analysis confirms the embedding of Co_3O_4 NPs in the g-C_3N_4 NSHs and the deposition of Ag NPs in the GC nanoheterostructure, forming an effective GCA nanoheterostructure. The high-resolution TEM (HRTEM) investigation for GCA (Fig. 3c) reveals two different lattice constants of 0.244 and 0.235 nm, belonging to the (311) and (111) crystal planes of Co_3O_4 and Ag

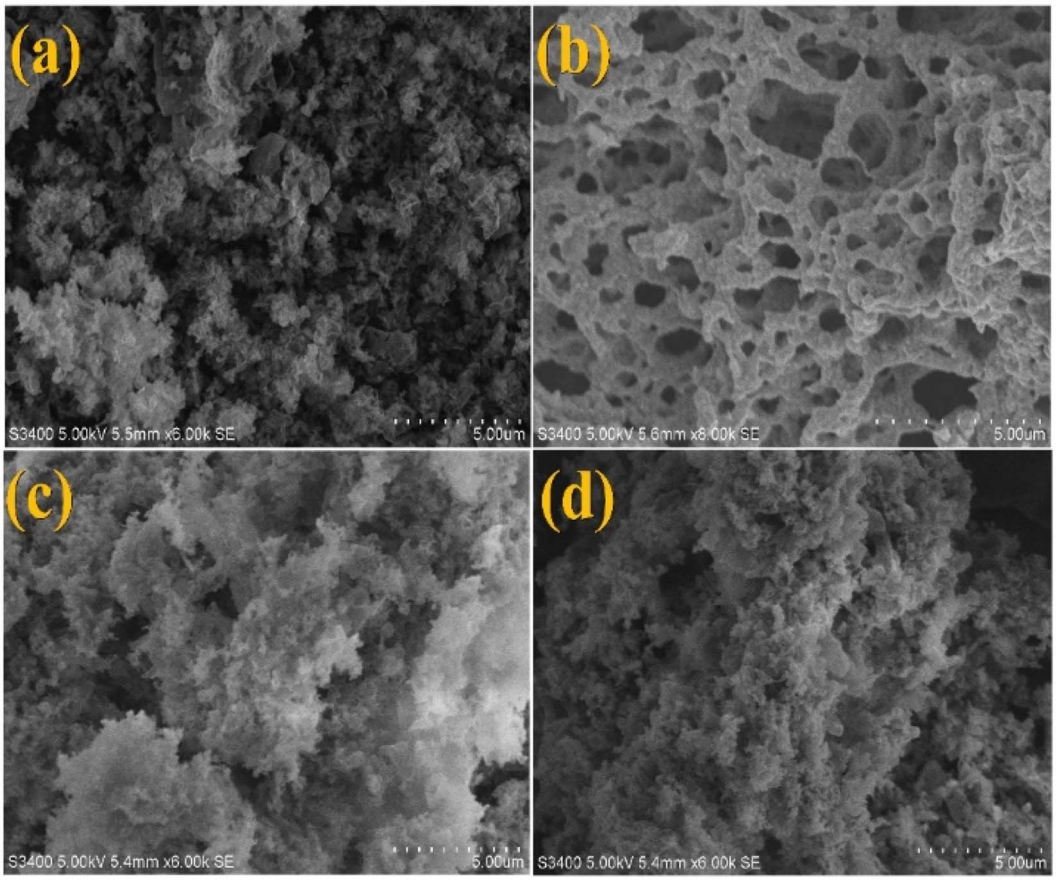

Fig. 2 (a) SEM images of (a) g-C_3N_4, (b) Co_3O_4, (c) GC, and (d) GCA photocatalysts.

NPs, respectively, embedded in layers of g-C_3N_4 NSHs. The HRTEM image discloses an intimate interface connection between the g-C_3N_4 NSHs and Co_3O_4 and Ag NPs, indicating stable heterojunction formation and promoting faster electron transportation and enhanced Ag^0 oxidation.[21] The presence and homogeneous distribution of C, N, O, Co, and Ag elements were confirmed by TEM-EDX elemental mapping (Fig. S1 and 3d). The corresponding EDX spectrum further verifies the elemental composition of the GCA nanocomposite, with Ag contributing ~1.9 at% (12.5 wt%). The relatively low atomic fraction but uniform spatial distribution of Ag confirms its highly dispersed nature on the GC surface, in good agreement with the weak Ag (111) diffraction peak observed in XRD analysis. The different comparison of the elemental distribution of the Ag and O elements confirms the exclusive production of metallic Ag^0 NPs on the surface of the GC nanocomposite. This finding is in line with XRD results as well.

3.3. Surface study

XPS analysis was performed to investigate the elemental surface and bonding behaviour of the studied samples. Fig. 4a displays the XPS survey spectra of the GCA sample, revealing the purity of the sample where no other element was detected other than Co, Ag, N, O, and C. High-resolution XPS of all the elements was investigated. Initially, the C 1s core level was calibrated at 284.6 eV as a reference. Fig. 4b shows the HRXPS spectrum of the C 1s core level, which was fitted into three peaks: 284.6 eV is the energy level associated with accidental carbon found on the surface of g-C_3N_4 (sp^2 C–C and C=C); 286.3 eV refers to sp^3 coordinated carbon bonds ($C(N)_3$/C–O) species, while 288.07 eV is N-sp^3 carbon (N–C=N) in the *s*-triazine ring units.[46–48] The N 1s core level spectra (Fig. 4c) exhibited three peaks located at 398.8, 400.1, and 401.5 eV, which represent sp^2-bonded nitrogen in C=N–C, N–$(C)_3$, and (C–N–H) groups, respectively.[46] The HRXPS spectrum of Co 2p showed two spin–orbit peaks of Co $2p_{3/2}$ and Co $2p_{1/2}$ positioned at 780.3 and 795.8 eV, respectively, and two satellite peaks are also present at about 784.6 and 801.7 eV (Fig. 4d). These peaks and satellites are attributed to Co^{3+} ions corresponding to the Co_3O_4 phase.[25,49] The corresponding O 1s HRXPS spectrum exhibited two distinct peaks (Fig. 2e). One peak is observed at 529.7 eV and is primarily attributed to the oxygen lattice in Co_3O_4. The other peak at 530.9 eV corresponds to $^-$OH species on the surfaces due to physically and chemisorbed oxygen.[50] Fig. 4f depicts the HRXPS spectrum of Ag 3d, which presents two spin–orbit peaks, Ag $3d_{5/2}$ and Ag $3d_{3/2}$, positioned at 368.0 and 374.0 eV, respectively. The spin–orbit splitting of the coupled 3d is 6.0 eV, corresponding to the metallic Ag^0 species,[51] indicating the presence of metallic silver on the surface of the GC nanocomposite.

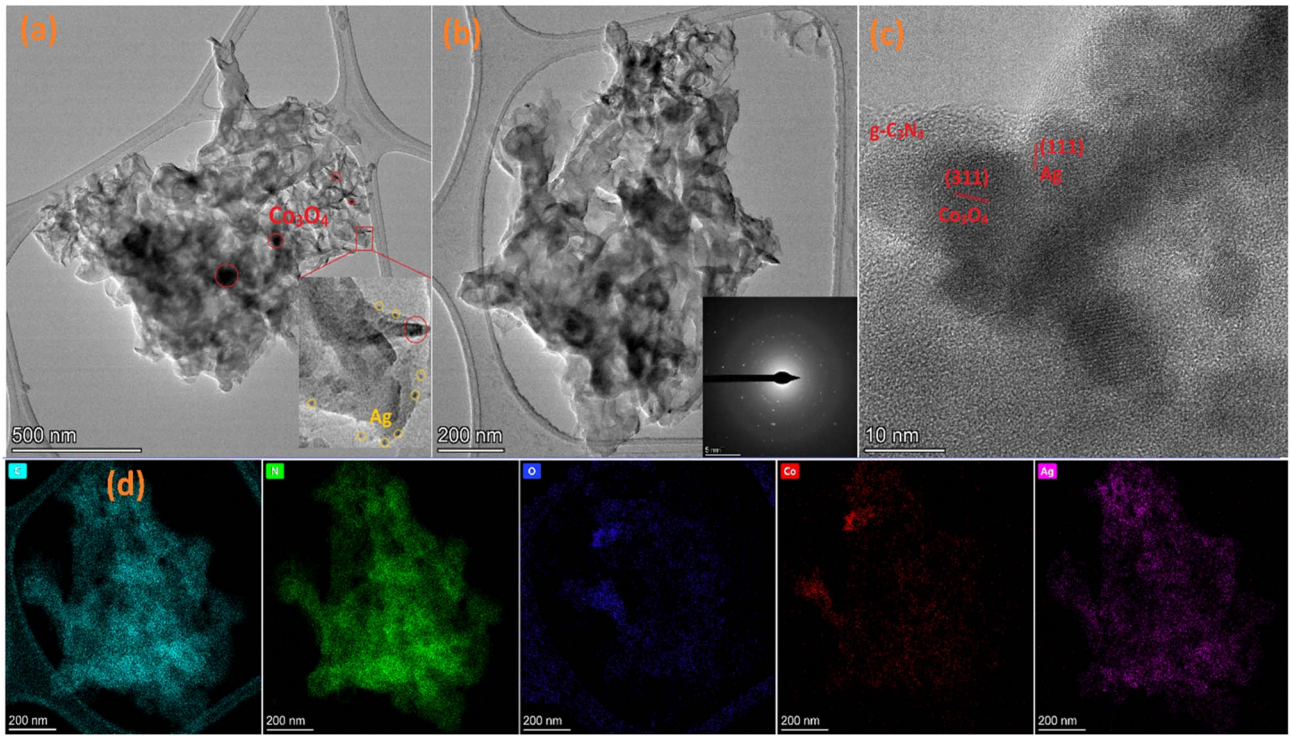

Fig. 3 (a and b) TEM and SAED images, (c) HRTEM image, and (d) elemental mapping images of the prepared GCA sample.

3.4. Antibacterial studies

Using a microtiter broth dilution study, the MIC and MBC concentrations of the studied photocatalysts were calculated to measure the antibacterial activity against the selected MDR isolates. In general, the MIC of the studied photocatalysts was found to be 140 μg mL^{-1} for all three tested MDR isolates.

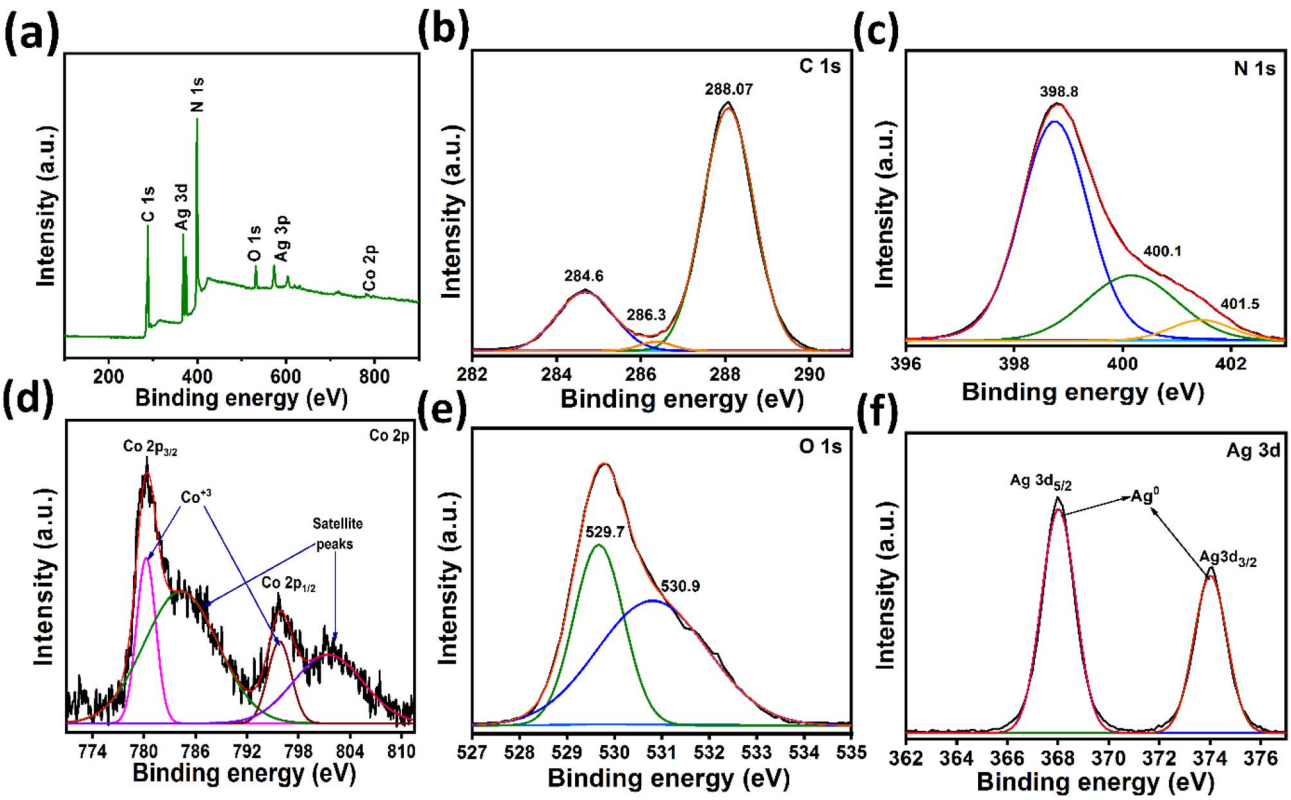

Fig. 4 (a) XPS survey spectrum; HRXPS spectra of (b) C 1s, (c) N 1s, (d) Co 2p, (e) O 1s, and (f) Ag 3d core levels of the GCA nanocomposite.

However, the MBC values were two times higher (280 μg mL^{-1}) than the MIC values. To determine the photocatalytic disinfection susceptibility of the MDR isolates, MDR-MRSA was used as a representative bacterial strain. The bacteria were treated with the studied photocatalysts at various concentrations, specifically MIC and MBC, and subjected to photo-irradiation during controlled incubation. Untreated bacterial strains continued to grow with time. In contrast, neither MDR-MRSA strains exposed to MIC concentrations of pure G and C, binary GC, and ternary GCA nanocomposite after 420, 360, 300, and 180 minutes of incubation (Fig. 5a) nor MDR-MRSA strains treated with MBC concentrations after 360, 300, 180, and 90 minutes demonstrated any growth (Fig. 5b), respectively. The diminished antibacterial activity of the GCA nanocomposite in the absence of light showed a slight lag phase attributed to the activity from Ag NPs. This suggests that the antibacterial activity of GCA nanocomposites is minimal under dark conditions, and the developed composite is not intrinsically hazardous. The compilation and comparison of antimicrobial activity in the recent literature with this study are presented in Table S1, which confirms this study's superior activity. The GCA sample was also subjected to five successive photocatalytic disinfection cycles, with catalyst recovery and reutilization following each cycle. Fig. S2 illustrates that GCA maintained robust bactericidal efficacy across all cycles, attaining total MRSA inactivation in each instance, accompanied by only a moderate rise in the necessary irradiation duration. No bacterial regrowth was seen after any cycle, confirming persistent bactericidal effectiveness. The minor reduction in antibacterial efficacy from cycle I to cycle V can be ascribed to partial surface fouling by bacterial remnants, slight photocatalyst loss during recovery, or diminished availability of active surface sites during repeated utilisation.

The improved photocatalytic disinfection activity of the GCA nanocomposite over pristine g-C_3N_4 and Co_3O_4 and the binary GC nanocomposite is due to many factors, especially the ability of the GCA nanocomposite to harvest the maximum light wavelength range for the generation of a large number of charge carriers. Moreover, these carriers must have a long lifetime and a minimum recombination rate. These optical characteristics of the GCA and other samples were investigated using DRS UV-Vis and PL analyses. Fig. 6a depicts the light absorption characteristics of all studied samples and confirms that all can absorb light radiation in the visible range. Combining Co_3O_4 NPs with g-C_3N_4 NSHs significantly enhanced the absorption capacity in comparison with the pristine g-C_3N_4 NSHs. Interestingly, the inclusion of Ag metal in the composites resulted in a redshift and an absorption peak centred at 580 nm, potentially attributed to the excitation of the SPR effect of the Ag NPs.[52] This phenomenon consequently improved the photocatalytic efficiency of the GCA nanocomposite, which aligns with previous research findings.[52,53] Therefore, the improved photocatalytic disinfection by the GCA sample is mainly attributed to the boosted light absorption by the plasmonic effect. On the other hand, Fig. 6b shows that the PL intensity of GCA is the lowest intensity compared with the pristine sample and the binary composite, revealing negligible recombination of the

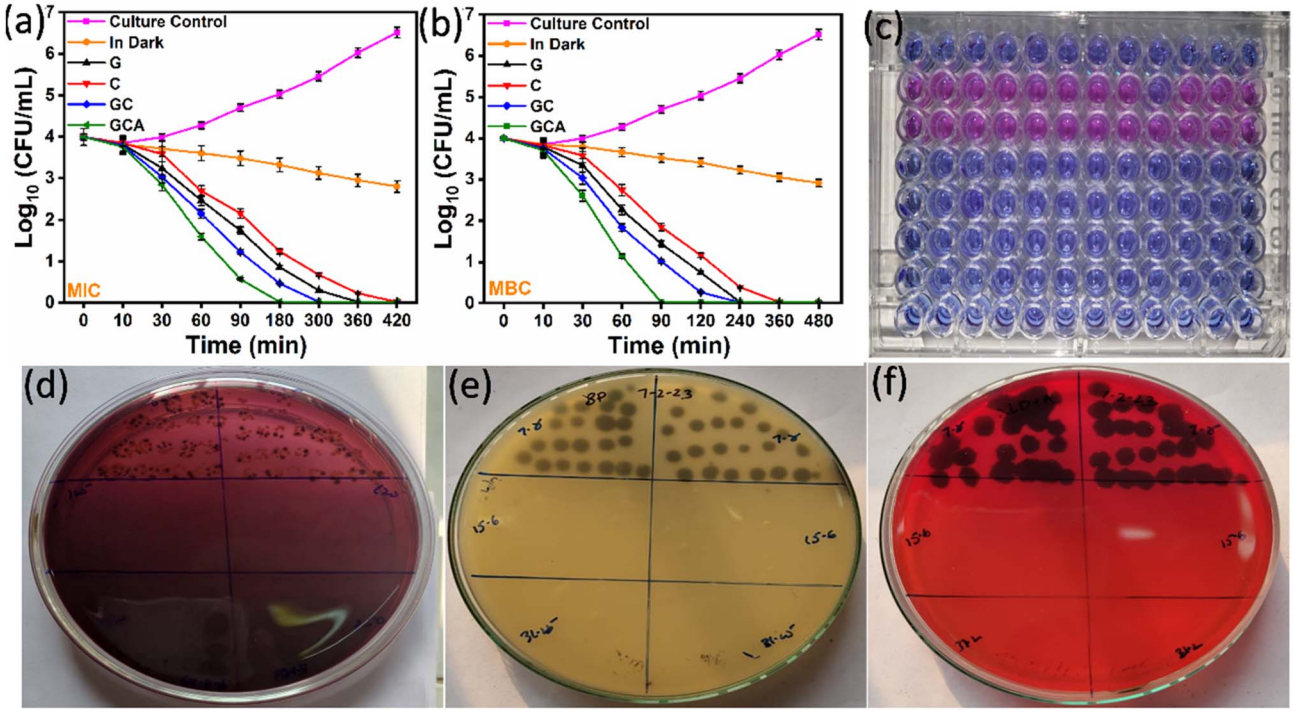

Fig. 5 Photocatalytic disinfection activity of the samples at two concentrations: (a) MIC and (b) MBC; (c) determination of MIC blue colored wells represents no bacterial growth and pink colored wells represents bacterial growth. MBC was determined in *E. coli*, *S. aureus,* and *Salmonella Enteritidis* for (d) EMB, (e) BP, and (f) XLD agars, respectively.

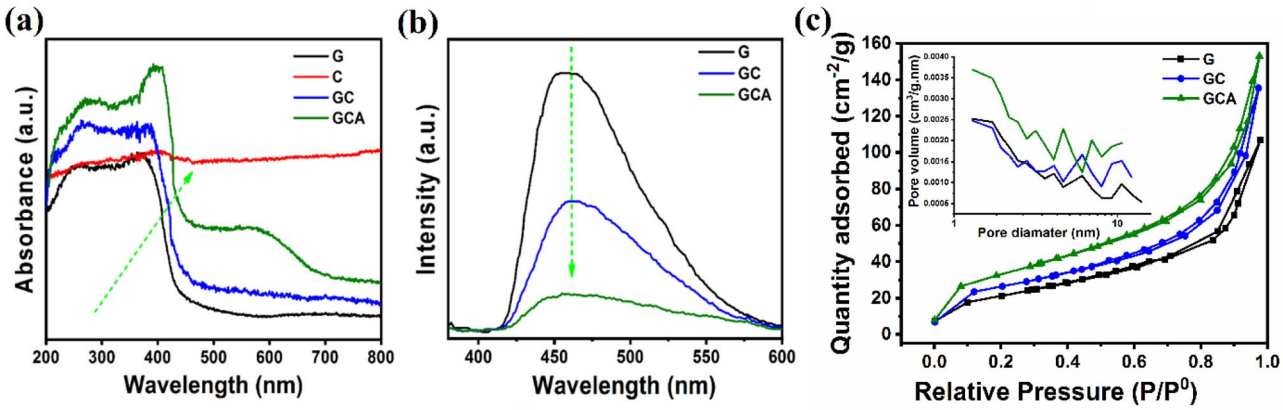

Fig. 6 (a) DRS UV-Vis, (b) PL spectra, and (c) BET specific surface areas of prepared samples.

photogenerated e^-/h^+ pairs, which favours an efficient photocatalytic performance.[54]

The G, GC, and GCA samples' surface area and porosity were assessed using nitrogen adsorption–desorption techniques. The mesoporous character of all samples is confirmed by type-IV isotherms with distinct hysteresis loops at intermediate to high relative pressures ($P/P^2 > 0.4$), as seen in Fig. 6c. The Brunauer–Emmett–Teller (BET) specific surface areas show a progressive enhancement upon composite formation, increasing from 75.3 $m^2\ g^{-1}$ (G) to 95.2 $m^2 g^{-1}$ (GC) and 103.5 $m^2\ g^{-1}$ (GCA). The pore size distribution analysis (inset of Fig. 6c) reveals that the GCA has higher nitrogen uptake across all pressures, indicating enhanced pore capacity and accessibility. The inset of Fig. 6c shows prominent 2–10 nm mesopores, which are good for photocatalytic antibacterial activity. The GCA heterostructure reduces particle agglomeration and enhances interfacial porosity, creating a hierarchical mesoporous architecture. The increased surface area and mesoporosity improve bacterial adsorption, active-site accessibility, and ROS diffusion, which, along with excellent S-scheme charge separation, make GCA a more effective photocatalytic disinfection option than G and GC.

3.5. The mechanism of action

Microbial annihilation driven by illumination has various advantages, functioning through oxidative harm initiated by generating ROSs such as $^{\bullet}OH$, $^{\bullet}O_2$, $^1O_2$, *etc.* This process is known as photodynamic therapy, and each ROS has its own redox potential value for its production.[55] As a result, measuring the VB maximum (VBM) and CB minimum (CBM) to determine the photocatalyst's ability to produce one or more ROSs for antibacterial activation under LED light is critical in understanding the photocatalytic disinfection mechanism by the targeted nanocomposite towards the selected bacterial strains. From the above DRS-UV-vis analysis (Fig. 6a), a Tauc plot was calculated to examine the bandgap values of G and C samples (Fig. 7a).[56] First, the optical bandgap (E_g) for each sample was extracted from the Tauc plots (Fig. 7a) by plotting $(\alpha h\nu)^{1/n}$ against the photon energy ($h\nu$). For g-C_3N_4, an exponent of $n = 2$ was used, identifying its indirect transition nature, while $n = 1/2$ was applied for the direct transition of Co_3O_4. The E_g values were determined by extrapolating the linear portion of the curve to the abscissa, yielding 2.7 eV and 2.06 eV, respectively. Subsequently, these experimental values were integrated into the empirical eqn (1) and (2) to calculate the absolute energy levels relative to the Normal Hydrogen Electrode (NHE):

$$\mathrm{VBM} = \chi - E_\mathrm{H} + 0.5E_\mathrm{g} \quad (1)$$

$$\mathrm{CBM} = \mathrm{VBM} - E_\mathrm{g} \quad (2)$$

Here, χ represents the geometric mean of the absolute electronegativity of the constituent atoms (4.73 eV for g-C_3N_4 and 5.908 eV for Co_3O_4),[25,57] and E_H is the energy of free electrons on the hydrogen scale (4.5 eV). By substituting the Tauc-derived E_g into these eqn (1) and (2), the VBMs were calculated to be +1.58 eV and +2.43 eV, with corresponding CBMs at −1.12 eV and +0.37 eV for g-C_3N_4 and Co_3O_4, respectively, to ensure that the predicted band alignments are grounded in the specific optical response of the synthesised materials. Fig. 7d shows the band diagram before their junction. The estimated type of the heterojunction, the charge migration pathway, and the active sites responsible for producing the ROSs involved in the efficient antibacterial activity of the GCA nanocomposite were investigated using XPS surface analysis and an ESR trapping agent experiment. HR-XPS of the pristine g-C_3N_4 and Co_3O_4 before the junction was investigated, and the N 1s and Co 2p core levels are shown in Fig. 7b and c. After the coupling of the g-C_3N_4 NSHs with Co_3O_4 NPs, the N 1s core level showed a slight positive shift (Fig. 7b), whereas the Co 2p core level had a slight negative shift (Fig. 7c). This positive shift of the N 1s core level indicates the electron transfer from the g-C_3N_4 interface into Co_3O_4, forming a positive charge layer on the surface of the g-C_3N_4 NSHs. In contrast, the negative shift of the Co 2p indicates the formation of a negative charge layer on the interface of the Co_3O_4 NPs. Hence, combining g-C_3N_4 and Co_3O_4 results in a nanoscale heterojunction. This junction created a sufficient space charge layer and generated an internal electric field (IEF) directed from g-C_3N_4 to Co_3O_4. This IEF causes the energy

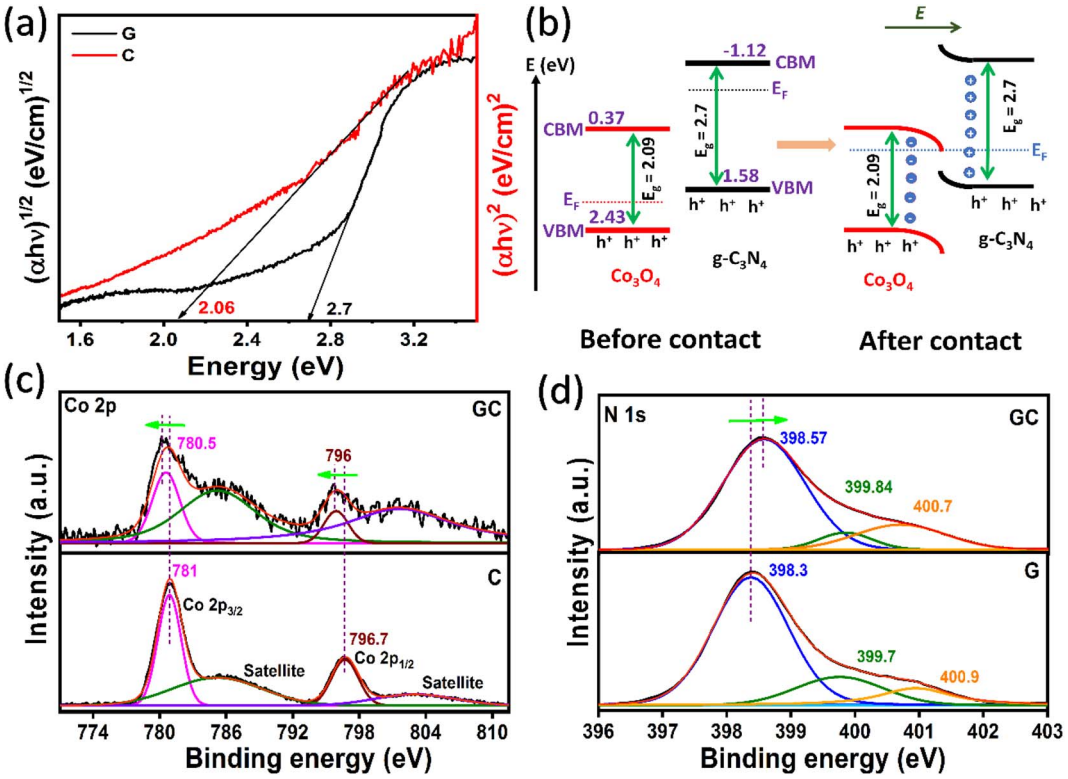

Fig. 7 (a) Tauc plots of g-C_3N_4 and Co_3O_4, (b) energy band diagrams of g-C_3N_4 and Co_3O_4 before and after the contact, HRXPS spectra of (c) Co 2p and (d) N 1s core levels of pure Co_3O_4, g-C_3N_4, and GC nanocomposite.

bands of g-C_3N_4 to bend upward and those of Co_3O_4 to bend downward; hence, a strong interface interaction between g-C_3N_4 and Co_3O_4 indicates S-scheme heterojunction formation (Fig. 7e).

Under light irradiation, the charge pathway is initiated with electrons excited from the VBs of g-C_3N_4 and Co_3O_4 into their CBs. The photoinduced electrons will accumulate on the CB of g-C_3N_4 due to its upward bending. This CB will work as the active site for the production of superoxide radicals ($^{\bullet}O_2^-$) as its potential is more negative than the $O_2/^{\bullet}O_2^-$ standard potential (-0.046)[25] (Fig. 8a). Simultaneously, the photogenerated holes will accumulate on the VB of Co_3O_4 due to the downward bending of its VB. This VB will work as the active site for the production of hydroxide radicals ($^{\bullet}OH$) because its potential is more positive than the $OH/^{\bullet}OH$ standard potential (+1.99).[25] Meanwhile, the electrons on the CB of Co_3O_4 and the holes on the VB of g-C_3N_4 will be recombined at the heterojunction interface, where their potential levels cannot generate $^{\bullet}O_2^-$ ($O_2/^{\bullet}O_2^- = -0.046$) and $^{\bullet}OH$ ($OH/^{\bullet}OH = +1.99$), respectively (Fig. 8a).

When Ag NPs are deposited on the g-C_3N_4/Co_3O_4 nanocomposite surface, the N 1s and the Co 2p core levels of the GCA composite (Fig. 4c and d) showed slight positive and negative shifts in comparison with N 1s and the Co 2p core levels of the GC composite (Fig. 7c and d), respectively. These shifts indicated the strong interaction and interfacial contact between Ag and the g-C_3N_4 NSHs and Co_3O_4 NPs in the GCA composite. According to the previous studies, g-C_3N_4 and Co_3O_4 are n-type and p-type semiconductors, respectively,[21,30,31] and Ag has a Fermi level at +0.4 eV *vs.* NHE.[58] Herein, Ag NPs on the GCA S-scheme system would play two roles: On the one side, the Ag NPs will contact with g-C_3N_4, forming a Schottky barrier at the interface of Ag/g-C_3N_4. Hence, upon light irradiation, the Ag NPs will work as an electron sink for the accumulated electrons on the CB of g-C_3N_4 due to the surface plasmon resonance effect and the lower Fermi level of the Ag NPs than the n-type g-C_3N_4.[59,60] This Ag/g-C_3N_4 junction would reduce the chance of the recombination rate of the e^-/h^+ pair in the GCA S-scheme system. Herein, the Ag NPs will work as the active site for the production of $^{\bullet}O_2^-$ (Fig. 8b). On the other side, Ag NPs will contact the p-type Co_3O_4, resulting in a Schottky barrier at the interface of Ag/Co_3O_4. At this junction, the Fermi level of Ag NPs is higher than the Fermi level of the p-type Co_3O_4; hence, due to the Schottky junction and the SPR effect, the photogenerated e^-/h^+ pairs tend to shift toward more negative redox potentials.[61,62] Therefore, the electrons will accumulate on the CB of Co_3O_4 and recombine with holes on the VB of g-C_3N_4 as the CB of Co_3O_4 is downward-pinned due to the junction formation with g-C_3N_4. Hence, the lifetime of the holes on the VB has been prolonged to be the active site for the production of $^{\bullet}OH$ and accelerating the photocatalytic reaction (Fig. 8b). In contrast, the Ag NPs in the junction would function as electron mediators promoting the charge carrier transfer and separation processes in the GCA S-scheme system.[30,31,63,64] The photogenerated holes and ROSs such as $^{\bullet}OH$ and $^{\bullet}O_2^-$ are very powerful, reactive, and non-selective, which can result in the oxidative modification of

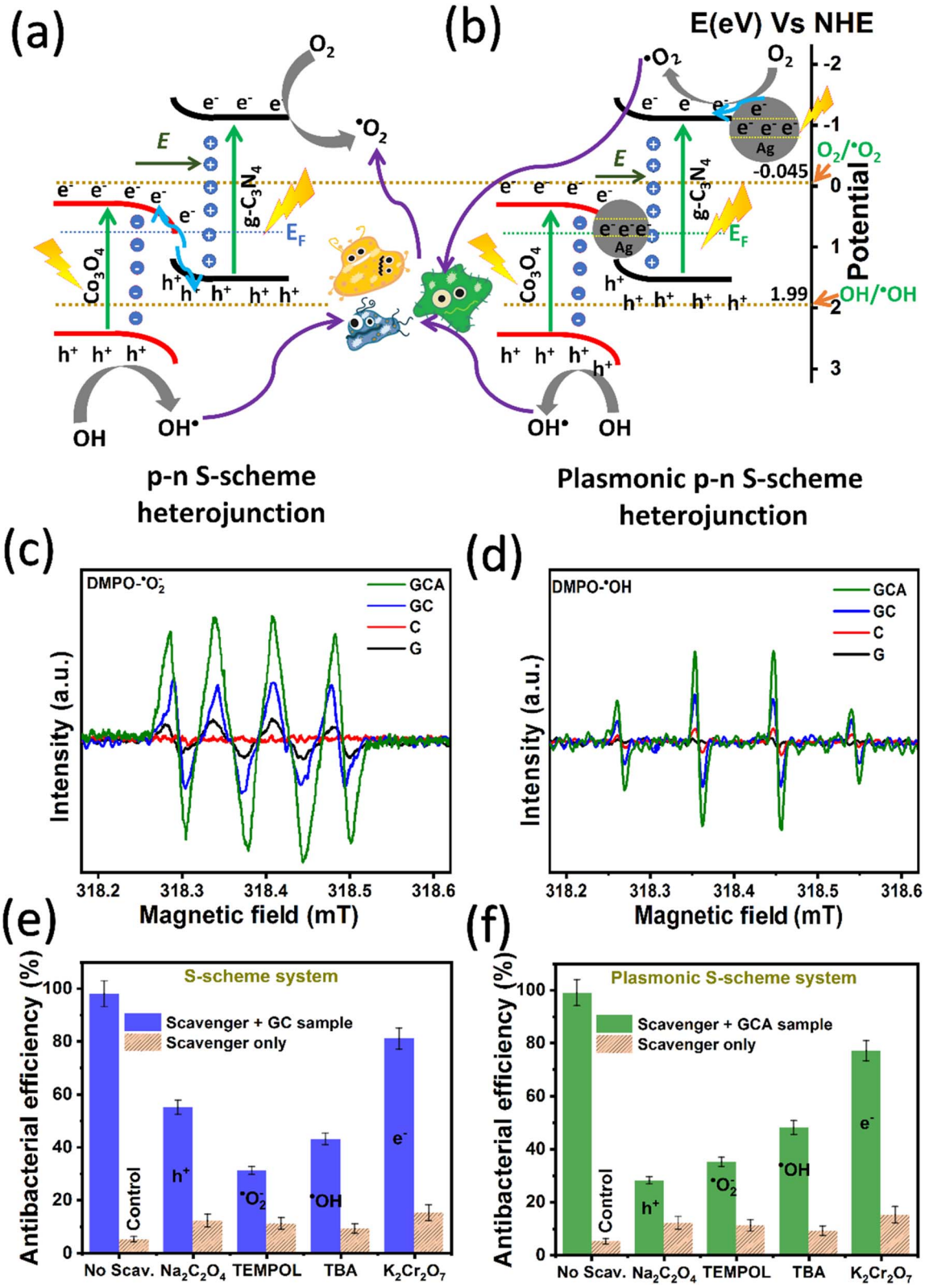

Fig. 8 Photocatalytic antibacterial disinfection mechanism for the (a) S-scheme GC and (b) plasmonic S-scheme GCA nanocomposites; ESR spectra of (c) DMPO-$^{\bullet}O_2^-$ and (d) DMPO-$^{\bullet}$OH for all samples under LED illumination; scavenging experiment of photocatalytic antibacterial efficiency over (e) GC and (f) GCA nanocomposites.

proteins, lipids, and DNA. The membrane lipid peroxidation results in cell membrane destruction, leading to the production of malonaldehydes and the release of cellular contents.[65,66] The intracellular biomacromolecules undergo oxidative reactions, leading to permanent damage and ultimately resulting in cell mortality.

The ESR measurements were performed to validate the generation of $^{\bullet}OH$ and $^{\bullet}O_2^-$ on the GCA heterostructure and confirm the construction of the S-scheme heterojunction. The investigations were carried out by monitoring the formation of $^{\bullet}OH$ and $^{\bullet}O_2^-$ throughout the photocatalytic process using 5,5-dimethyl pyrroline *N*-oxide (DMPO) as the free radical scavenging mediator in both water and alcohol solutions, respectively. Fig. 8c and d shows the ESR signals for the G, C, GC, and GCA samples in both water and alcohol solutions. The study's findings demonstrated strong ESR spectra in both aquatic media for the GC and GCA composites, suggesting the generation of $^{\bullet}OH$ and $^{\bullet}O_2^-$ by these composites. The pure G sample exhibited a weak signal in the alcohol medium and no signal in the aqueous medium. In contrast, the C sample showed the opposite behaviour. This suggests that the G sample only produced $^{\bullet}O_2^-$ while the C sample produced $^{\bullet}OH$. These differences can be attributed to the higher CB and VB redox potentials of the G and C samples. The results propose that the active site for accumulated electrons in the GC heterostructure is the CBM of G, as its CBM exceeds the standard redox potential for $O_2/^{\bullet}O_2^-$ production (-0.045). Similarly, the VBM of C is identified as the active site for generated holes, with its redox potential surpassing that of the standard potential of $OH/^{\bullet}OH$ (+1.99 V). These data suggest that the charge pathway between G and C does not follow the usual type II heterojunction. Rather, the unique S-scheme heterojunction could explain the enhanced antibacterial performance of GCA. The ESR signal of the GCA was greater than that of the GC due to the surface plasmon resonance effect of the deposited Ag-NPs on the surface of the GC sample. The presence of the Ag-NPs boosted the charge transit in the GCA heterostructure as it worked as an electron mediator. Simultaneously, Ag-NPs functioned as a photoinduced electron trap and worked as an active site for producing more $^{\bullet}O_2^-$. As a result, the ESR findings back up the XPS results regarding the charge migration pathway in the GC and GCA composites following the S-scheme heterojunction. Furthermore, active species trapping studies were carried out to confirm the predominant free radicals for photocatalytic disinfection and to identify the antibacterial mechanism. The study followed the same procedure described in the experimental section of photocatalytic disinfection. Herein, we introduced the relevant species trapping agents before incubation, such as 1 mM 4-hydroxy-2,2,6,6-tetramethylpiperidinyloxy (TEMPOL), potassium dichromate ($K_2Cr_2O_7$), *tert*-butanol (TBA), and sodium oxalate ($Na_2C_2O_4$) to detect the $^{\bullet}O_2^-$, e^-, $^{\bullet}OH$, and h^+ active species, respectively. The results of each active species-trapping agent were measured in CFU, and their toxicities were calibrated as the controls; Fig. 8e and f display their corresponding efficiencies. The antibacterial activity in the binary GC S-scheme system and the ternary GCA plasmonic S-scheme system was varied with the addition of the identifying active species capturer. For the binary GC composite, $^{\bullet}O_2^-$ was the main dynamic species, followed by $^{\bullet}OH$ (Fig. 8e), which aligns with the ESR findings, where the spectrum intensity of $^{\bullet}O_2^-$ is higher than $^{\bullet}OH$. This result also confirms the construction of an S-scheme junction in the GC nanoheterostructure. However, e^- and h^+ were minor free radicals in this S-scheme system.

On the other hand, h^+ was the main dynamic species in the presence of the ternary GCA composite, indicating an increase in the number of photogenerated e^-/h^+ pairs and a reduction in their recombination rate. This result reveals that Ag NPs acted as electron mediators, prolonging the charge separation. Moreover, $^{\bullet}O_2^-$ was also dominated as a remarkably active species contributor. The large production of $^{\bullet}O_2^-$ in the GCA composite due to the SPR effect, which increased the number of accumulated e^- on the CB of g-C_3N_4 NSHs by the hot e^- transferred over the Schottky junction between the g-C_3N_4 NSHs and Ag NPs, confirming the formation of a plasmonic S-scheme heterojunction in the GCA composite. Similarly to the GC composite, the contribution of $^{\bullet}OH$ is lesser than $^{\bullet}O_2^-$, which aligns with the ESR finding. Furthermore, electrochemical impedance spectroscopy (EIS) was utilised to examine the interfacial charge-transfer properties and to clarify the function of the S-scheme heterojunction in improving charge separation.[54] The Nyquist plots (Fig. S3) demonstrate that the pure g-C_3N_4 possesses the biggest semicircle diameter, signifying elevated charge-transfer resistance and fast recombination of photogenerated electron–hole pairs. The semicircle radius diminishes upon coupling with Co_3O_4 (GC S-scheme heterojunction), indicating increased interfacial contact and a moderate enhancement in charge movement. The plasmonic S-scheme heterojunction GCA composite exhibits the smallest semicircle diameter of all samples, indicating the lowest charge-transfer resistance and the most effective interfacial charge transport.

In conclusion, constructing a plasmonic S-scheme heterostructure using 2D materials enhanced the light absorption and charge separation, resulting in increased e^-/h^+ generation, separation, and selective redox potential, thereby improving the production of ROSs. Ultimately, the synthesised plasmonic S-scheme g-C_3N_4–Co_3O_4–Ag nanocomposite exhibited considerable efficacy against drug-resistant bacteria, proving suitable for disease treatment.

4. Conclusion

This work presents a rational design strategy for a 2D plasmonic nanocomposite comprising g-C_3N_4 NSHs, Co_3O_4, and Ag NPs. The nanocomposite exhibits excellent antibacterial properties when exposed to LED light. The successful construction of the ternary heterostructure was verified using various characterisation methods, including XRD, TEM, SEM, XPS, DRS UV-Vis, and PL analyses. The S-scheme charge migration pathway was investigated using XPS, ESR, and species-trapping agent techniques, which verified the establishment of an effective charge separation mechanism inside the GC and GCA nanocomposites. The inclusion of Ag NPs resulted in the occurrence of the SPR effect, which improved light absorption and the separation of charges. Under LED light irradiation, the GCA nanocomposite demonstrates

remarkable antibacterial activity against MRSA, NTS, and EAEC, with consistent MIC and MBC values recorded at 140 and 280 μg mL^{-1} across all tested strains, respectively. The photocatalytic disinfection efficacy was evaluated, highlighting the nanocomposite's potential for combating drug-resistant bacteria. The enhanced antibacterial activity of the GCA nanocomposite over binary and pristine samples emphasises the synergistic effects of the plasmonic and S-scheme heterojunction, addressing the critical need for innovative approaches to combat drug-resistant organisms. Importantly, minimal antimicrobial effects are detected in the absence of visible light, demonstrating the safety of the developed composite for practical applications. The GCA nanocomposite's excellent visible-light-driven antibacterial activity, stability, and low dark toxicity demonstrate its application in water disinfection systems, antimicrobial surface coatings, and medical or hospital applications that require light-triggered sterilisation. These findings suggest a possible framework for developing enhanced photocatalytic antibacterial materials to combat antibiotic-resistant organisms.

Author contributions

Sanaa Abdu Kaid: formal analysis, data curation, methodology, writing – original draft, discussion, and investigation. Khaled Alkanad: conceptualization, data curation, methodology, writing – original draft, discussion, investigation, proofreading, writing – reviewing, editing, and formal analysis. Nael Abutaha: methodology, supporting acquisition, project administration, writing – reviewing, and editing. Fahd A. Al-Mekhlafi: resources, discussion, reviewing, and editing. Padikkamannil Abishad: resources, methodology, formal analysis, writing – reviewing, and editing. Mohammed A. Bajiri: discussion, formal analysis, data curation, writing – reviewing, and editing. Maged Alkanad: methodology, resources, discussion, writing – reviewing, and editing. Mohamed Masri: formal analysis, reviewing, and editing. Yusuf Olatunji Waidi: discussion, reviewing, and editing. Kalappa Prashantha: discussion, reviewing, and editing. N. Upendra: supervision, resources, investigation, discussion, reviewing, and editing. N. K. Lokanath: conceptualization, resources, supervision, discussion, writing – reviewing, and editing.

Conflicts of interest

There are no conflicts to declare.

Data availability

The data utilised in this study will be made available upon request.

Supplementary information (SI) is available. See DOI: https://doi.org/10.1039/d5na00943j.

Funding

This project was funded by the Ongoing Research Funding program (ORF-2025-757), King Saud University, Riyadh, Saudi Arabia.

Acknowledgements

The authors express their sincere appreciation to the Ongoing Research Funding program (ORF-2025-757), King Saud University, Riyadh, Saudi Arabia.

References

1 M.-j. Medina, H. Legido-Quigley and L. Y. Hsu, *Global Health Security: Recognizing Vulnerabilities, Creating Opportunities*, 2020, pp. 209–229.
2 J. A. Johnson, *Crit. Care*, 2021, 82–83.
3 WHO, World Health Organization Report, *Antimicrobial resistance surveillance in Europe 2022–2020 data*, 2022.
4 M. Suleiman, A. Alali, N. Aljayyousi, K. Alkanad, N. Elkhatatneh, M. Almaqashah, A. Zarrouk and A. Abu-Rayyan, *Morrocan J. Chem.*, 2023, **11**(2), 434–443.
5 J. M. V. Makabenta, A. Nabawy, C.-H. Li, S. Schmidt-Malan, R. Patel and V. M. Rotello, *Nat. Rev. Microbiol.*, 2021, **19**, 23–36.
6 A. AlAli, M. Alkanad, K. Alkanad, A. Venkatappa, N. Sirawase, I. Warad and S. A. Khanum, *Bioorg. Chem.*, 2025, 108422.
7 H. Shen, C. Jiang, W. Li, Q. Wei, R. A. Ghiladi and Q. Wang, *ACS Appl. Mater. Interfaces*, 2021, **13**, 31193–31205.
8 S. Alfei, G. C. Schito, A. M. Schito and G. Zuccari, *Int. J. Mol. Sci.*, 2024, **25**, 7182.
9 N. Talreja, D. Chauhan and M. Ashfaq, *Antibiotics*, 2023, **12**, 398.
10 S. N. Kulkarni, R. R. Nath, K. Alkanad, A. Amasegowda, S.-C. Ke and N. Lokanath, *J. Alloys Compd.*, 2025, 178876.
11 O. Ali, K. Alkanad, G. S. Shekar, A. Hezam and N. Lokanath, *Mater. Today: Proc.*, 2023, **92**, 796–800.
12 J. Murugaiyan, P. A. Kumar, G. S. Rao, K. Iskandar, S. Hawser, J. P. Hays, Y. Mohsen, S. Adukkadukkam, W. A. Awuah and R. A. M. Jose, *Antibiotics*, 2022, **11**, 200.
13 T. F. Qahtan, T. O. Owolabi, O. E. Olubi and A. Hezam, *Coord. Chem. Rev.*, 2023, **492**, 215276.
14 S. Hu and M. Zhu, *ChemCatChem*, 2019, **11**, 6147–6165.
15 M. Masri, K. Girisha, A. Hezam, T. F. Qahtan, K. Alkanad, F. Masri, K. Namratha and K. Byrappa, *Colloids Surf., C*, 2024, **2**, 100024.
16 Y. Wang, B. Ren, J. Z. Ou, K. Xu, C. Yang, Y. Li and H. Zhang, *Sci. Bull.*, 2021, **66**, 1228–1252.
17 M. Masri, K. Girisha, A. Hezam, K. Alkanad, T. F. Qahtan, Q. A. Drmosh, K. Prashantha, S. Manjunath, S. M. A. Kaid and K. Byrappa, *Nanoscale Adv.*, 2025, **7**(4), 1030–1047.
18 Y. Bao, S. Song, G. Yao and S. Jiang, *Sol. RRL*, 2021, **5**, 2100118.
19 Y. Li, S. Shu, L. Huang, J. Liu, J. Liu, J. Yao, S. Liu, M. Zhu and L. Huang, *J. Colloid Interface Sci.*, 2023, **633**, 60–71.
20 N. L. Reddy, V. N. Rao, M. Vijayakumar, R. Santhosh, S. Anandan, M. Karthik, M. Shankar, K. R. Reddy, N. P. Shetti and M. Nadagouda, *Int. J. Hydrogen Energy*, 2019, **44**, 10453–10472.
21 M. A. Bajiri, K. Alkanad, G. Alnaggar, G. C. Sujay Shekar, B. M. Al-Maswari, M. M. Abdullah, A. Al-khawlani,

N. K. Lokanath, B. Neppolian and H. S. Bhojya Naik, *Surf. Interfaces*, 2023, **42**, 103511.
22 Y. Olatunji Waidi, K. Alkanad, M. Abdullah Bajiri, T. F. Qahtan, A. Al-Aswad, T. N. Baroud, S. A. Onaizi and Q. Drmosh, *Chem.–Asian J.*, 2024, **19**, e202400822.
23 K. Yan, C. Mu, L. Meng, Z. Fei and P. J. Dyson, *Nanoscale Adv.*, 2021, **3**, 3708–3729.
24 F. Zhao and H. Ma, *Crystals*, 2023, **13**, 634.
25 K. Alkanad, A. Hezam, G. S. Sujay Shekar, Q. Drmosh, A. A. Kala, M. Q. AL-Gunaid and N. K. Lokanath, *Catal. Sci. Technol.*, 2021, **11**(9), 3084–3097.
26 G. S. Sujay Shekar, K. Alkanad, A. Hezam and N. Lokanath, *Int. Res. J. Eng. Tech.*, 2020, **7**, 194–196.
27 S. R. Yousefi, H. A. Alshamsi, O. Amiri and M. Salavati-Niasari, *J. Mol. Liq.*, 2021, **337**, 116405.
28 X. Huang, H. Cai, H. Zhou, T. Li, H. Jin, C. E. Evans, J. Cai and J. Pi, *Acta Biomater.*, 2021, **121**, 605–620.
29 A. Waris, M. Din, A. Ali, S. Afridi, A. Baset, A. U. Khan and M. Ali, *Open Life Sci.*, 2021, **16**, 14–30.
30 J. Wan, P. Xue, R. Wang, L. Liu, E. Liu, X. Bai, J. Fan and X. Hu, *Appl. Surf. Sci.*, 2019, **483**, 677–687.
31 D. Gogoi, A. K. Shah, M. Qureshi, A. K. Golder and N. R. Peela, *Appl. Surf. Sci.*, 2021, **558**, 149900.
32 T. Ni, H. Zhang, Z. Yang, L. Zhou, L. Pan, C. Li, Z. Yang and D. Liu, *J. Colloid Interface Sci.*, 2022, **625**, 466–478.
33 S. Dai, L. Xiao, Q. Li, G. Hao, Y. Hu and W. Jiang, *Sep. Purif. Technol.*, 2022, **297**, 121481.
34 J. J. Giner-Casares and L. M. Liz-Marzán, *Nano Today*, 2014, **9**, 365–377.
35 I. Ullah, K. Tahir, A. U. Khan, K. Albalawi, B. Li, A. A. El-Zahhar, V. Jevtovic, H. S. Al-Shehri, B. H. Asghar and M. M. Alghamdi, *Inorg. Chem. Commun.*, 2022, **141**, 109539.
36 E. Kargar and A. Meshkini, *J. Photochem. Photobiol., A*, 2024, **452**, 115577.
37 Fauzia, M. A. Khan, M. Chaman and A. Azam, *Sci. Rep.*, 2024, **14**, 6606.
38 B. Mohan, P. Abishad, P. R. Arya, M. Dias, V. K. Vinod, A. Karthikeyan, S. Juliet, N. V. Kurkure, S. B. Barbuddhe and D. B. Rawool, *Gut Pathogens*, 2024, **16**, 51.
39 S. Nazari, H. Alamgholiloo, E. Asgari, H. R. Moghaddam, H. N. Saleh, S. Parastar and A. Niapour, *J. Mol. Liq.*, 2022, **358**, 119227.
40 J. Jia, S. Giannakis, D. Li, B. Yan and T. Lin, *Sci. Total Environ.*, 2023, **901**, 166376.
41 S. A. Matboo, S. Nazari, A. Niapour, M. V. Niri, E. Asgari and S. A. Mokhtari, *Water Sci. Technol.*, 2022, **85**, 605–616.
42 Fauzia, M. A. Khan, A. Parveen, A. Almohammedi and A. Azam, *Opt. Quantum Electron.*, 2024, **56**, 1422.
43 A. Sheikhmohammadi, H. Alamgholiloo, M. Azarsa and E. Asgari, *J. Environ. Chem. Eng.*, 2025, 117332.
44 P. Abishad, M. Jayashankar, K. Namratha, B. Srinath, N. Kurkure, S. Barbuddhe, D. Rawool, J. Vergis and K. Byrappa, *Russ. J. Bioorg. Chem.*, 2023, 1–7.
45 K. B. Narayanan and N. Sakthivel, *Mater. Res. Bull.*, 2011, **46**, 1708–1713.
46 H. Shao, X. Zhao, Y. Wang, R. Mao, Y. Wang, M. Qiao, S. Zhao and Y. Zhu, *Appl. Catal., B*, 2017, **218**, 810–818.
47 L. Wang, M. Yu, C. Wu, N. Deng, C. Wang and X. Yao, *Adv. Synth. Catal.*, 2016, **358**, 2631–2641.
48 A. R. Z. Almotairy, B. M. Al-Maswari, K. Alkanad, N. Lokanath, R. Radhika and B. Venkatesha, *Heliyon*, 2023, **9**(8), e18496.
49 A. N. Naveen and S. Selladurai, *Phys. B*, 2015, **457**, 251–262.
50 C. Yan, G. Chen, J. Sun, X. Zhou and C. Lv, *Phys. Chem. Chem. Phys.*, 2016, **18**, 19531–19535.
51 L. Yang, C. Bo, R. Wu, S. Xu, Q. Li, Y. Ding and C. Gao, *Phys. Chem. Chem. Phys.*, 2023, **25**(24), 16371–16379.
52 X. Lü, J. Shen, Z. Wu, J. Wang and J. Xie, *J. Mater. Res.*, 2014, **29**, 2170–2178.
53 F. Ding, T. Ming, H. Zhang, Y. Gao, V. Dragutan, Y. Sun, I. Dragutan and Z. Xu, *Resour. Chem. Mater.*, 2022, **1**, 1–7.
54 A. H. Bashal, K. Alkanad, M. Al-Ghorbani, S. B. Aoun and M. A. Bajiri, *J. Environ. Chem. Eng.*, 2023, 109545.
55 Y. Nosaka and A. Y. Nosaka, *Chem. Rev.*, 2017, **117**, 11302–11336.
56 M. Q. Al-Gunaid, B. Shashikala, H. Gayitri, K. Alkanad, N. Al-Zaqri, A. Boshaala and F. H. Al-Ostoot, *Macromol. Res.*, 2022, **30**, 650–658.
57 M. M. Sanad, T. A. Taha, A. Helal and M. H. Mahmoud, *Environ. Sci. Pollut. Res.*, 2023, **30**, 60225–60239.
58 Y. Yang, Y. Guo, F. Liu, X. Yuan, Y. Guo, S. Zhang, W. Guo and M. Huo, *Appl. Catal., B*, 2013, **142**, 828–837.
59 F. Li, R. Zhao, B. Yang, W. Wang, Y. Liu, J. Gao and Y. Gong, *Int. J. Hydrogen Energy*, 2019, **44**, 30185–30195.
60 J. Qin, J. Huo, P. Zhang, J. Zeng, T. Wang and H. Zeng, *Nanoscale*, 2016, **8**, 2249–2259.
61 X. Gao, Z. Bai, S. Zhang, J. Liu and Z. Li, *RSC Adv.*, 2020, **10**, 45067–45075.
62 H. Chen, C. Xue, D. Cui, M. Liu, Y. Chen, Y. Li and W. Zhang, *RSC Adv.*, 2020, **10**, 15245–15251.
63 D. Lu, H. Wang, X. Zhao, K. K. Kondamareddy, J. Ding, C. Li and P. Fang, *ACS Sustain. Chem. Eng.*, 2017, **5**, 1436–1445.
64 B. Zhou, H. Hong, H. Zhang, S. Yu and H. Tian, *J. Chem. Technol. Biotechnol.*, 2019, **94**, 3806–3814.
65 B. Song, C. Zhang, G. Zeng, J. Gong, Y. Chang and Y. Jiang, *Arch. Biochem. Biophys.*, 2016, **604**, 167–176.
66 E. Cadenas and K. J. Davies, *Free Radical Biol. Med.*, 2000, **29**, 222–230.